



The R-Process Alliance: Spectroscopic Follow-up of Low-metallicity Star Candidates from the Best & Brightest Survey

Vinicius M. Placco^{1,2,15} , Rafael M. Santucci^{3,4} , Timothy C. Beers^{1,2} , Julio Chanamé^{5,6}, María Paz Sepúlveda^{5,6}, Johanna Coronado^{5,7}, Silvia Rossi⁸, Young Sun Lee⁹ , Else Starkenburg¹⁰, Kris Youakim¹⁰, Manuel Barrientos^{5,6}, Rana Ezzeddine^{2,11} , Anna Frebel^{2,11} , Terese T. Hansen¹² , Erika M. Holmbeck^{1,2} , Alexander P. Ji^{12,16} , Kaitlin C. Rasmussen^{1,2}, Ian U. Roederer^{2,13} , Charli M. Sakari¹⁴ , and Devin D. Whitten^{1,2}

¹ Department of Physics, University of Notre Dame, Notre Dame, IN 46556, USA; vplacco@nd.edu

² JINA Center for the Evolution of the Elements, USA

³ Instituto de Estudos Sócio-Ambientais, Planetário, Universidade Federal de Goiás, Goiânia, GO 74055-140, Brazil

⁴ Instituto de Física, Universidade Federal de Goiás, Campus Samambaia, Goiânia, GO 74001-970, Brazil

⁵ Instituto de Astrofísica, Pontificia Universidad Católica de Chile, Santiago, Chile

⁶ Millennium Institute of Astrophysics, Santiago, Chile

⁷ Max-Planck-Institut für Astronomie, Königstuhl 17, D-69117 Heidelberg, Germany

⁸ Instituto de Astronomia, Geofísica e Ciências Atmosféricas, Universidade de São Paulo, SP 05508-900, Brazil

⁹ Department of Astronomy and Space Science, Chungnam National University, Daejeon 34134, Republic of Korea

¹⁰ Leibniz Institute for Astrophysics Potsdam, D-14482 Potsdam, Germany

¹¹ Department of Physics and Kavli Institute for Astrophysics and Space Research, Massachusetts Institute of Technology, Cambridge, MA 02139, USA

¹² Observatories of the Carnegie Institution for Science, Pasadena, CA 91101, USA

¹³ Department of Astronomy, University of Michigan, Ann Arbor, MI 48109, USA

¹⁴ Department of Astronomy, University of Washington, Seattle, WA 98195-1580, USA

Received 2018 October 23; revised 2018 November 21; accepted 2018 November 21; published 2019 January 16

Abstract

We present results from an observing campaign to identify low-metallicity stars in the Best & Brightest Survey. From medium-resolution ($R \sim 1200\text{--}2000$) spectroscopy of 857 candidates, we estimate the stellar atmospheric parameters (T_{eff} , $\log g$, and $[\text{Fe}/\text{H}]$), as well as carbon and α -element abundances. We find that 69% of the observed stars have $[\text{Fe}/\text{H}] \leq -1.0$, 39% have $[\text{Fe}/\text{H}] \leq -2.0$, and 2% have $[\text{Fe}/\text{H}] \leq -3.0$. There are also 133 carbon-enhanced metal-poor (CEMP) stars in this sample, with 97 CEMP Group I and 36 CEMP Group II stars identified in the $A(\text{C})$ versus $[\text{Fe}/\text{H}]$ diagram. A subset of the confirmed low-metallicity stars were followed-up with high-resolution spectroscopy, as part of the R-process Alliance, with the goal of identifying new highly and moderately r -process-enhanced stars. Comparison between the stellar atmospheric parameters estimated in this work and from high-resolution spectroscopy exhibit good agreement, confirming our expectation that medium-resolution observing campaigns are an effective way of selecting interesting stars for further, more targeted, efforts.

Key words: Galaxy: halo – stars: abundances – stars: atmospheres – stars: carbon – stars: Population II – techniques: spectroscopic

Supporting material: machine-readable tables

1. Introduction

Very metal-poor (VMP; $[\text{Fe}/\text{H}]^{17} < -2.0$) stars are the *Rosetta Stones* of stellar astrophysics in the early universe. Encoded in the atmosphere of these low-mass, long-lived stars are the signatures of nucleosynthetic processes that could have occurred as early as a few tens of millions of years after the Big Bang (Alvarez et al. 2006). This provides a unique opportunity to witness not only the chemical and dynamical evolution of the Milky Way, but also to identify and distinguish between a number of possible scenarios for the enrichment of early star-forming gas clouds (Jeon et al. 2017; Chiaki et al. 2018).

It has long been recognized that metal-poor stars with overabundances of carbon relative to iron ($[\text{C}/\text{Fe}] > +0.7$) become more frequent for decreasing metallicities. The fractions of carbon-enhanced metal-poor (CEMP) stars increase

from 15%–20% for VMP stars to more than 80% for ultra metal-poor (UMP; $[\text{Fe}/\text{H}] < -4.0$) stars (Lee et al. 2013; Yong et al. 2013; Placco et al. 2014b; Yoon et al. 2018). The elemental-abundance patterns of CEMP stars are required in order to probe the nature of different progenitor populations responsible for the production of carbon and other elements (Placco et al. 2015b, 2016b). Moreover, recent studies (Norris et al. 2013) show that the majority of CEMP stars with $[\text{Fe}/\text{H}] < -3.0$ belong to the CEMP-no subclass, characterized by the lack of enhancements in their neutron-capture elements ($[\text{Ba}/\text{Fe}] < 0.0$). The brightest extremely metal-poor (EMP; $[\text{Fe}/\text{H}] < -3.0$) star in the sky, BD+44°493, with $[\text{Fe}/\text{H}] = -3.8$ and $V = 9.1$, is a CEMP-no star (Ito et al. 2013), and shares a common elemental-abundance signature with the recently discovered CEMP-no star with $[\text{Fe}/\text{H}] \lesssim -8.0$ (Keller et al. 2014; Bessell et al. 2015; Nordlander et al. 2017). This distinctive CEMP-no pattern has also been identified in high- z damped $\text{Ly}\alpha$ systems (Cooke et al. 2012), and is common among stars in ultra-faint dwarf galaxies, such as SEGUE-1 (Frebel et al. 2014). These observations suggest that CEMP-no

¹⁵ Visiting astronomer, Kitt Peak National Observatory.

¹⁶ Hubble Fellow.

¹⁷ $[\text{A}/\text{B}] = \log(N_{\text{A}}/N_{\text{B}})_{\star} - \log(N_{\text{A}}/N_{\text{B}})_{\odot}$, where N is the number density of atoms of a given element in the star (\star) and the Sun (\odot), respectively.

stars exhibit the nucleosynthesis products of the very first generation of stars (Hansen et al. 2016; Chiaki et al. 2017; Hartwig et al. 2018).

Bright VMP stars without C-enhancement are ideal targets for the high-resolution spectroscopic identification of new examples of the rare class of stars with moderate-to-large enhancements of elements associated with the rapid neutron-capture process (*r*-process), the so-called *r*-I ($+0.3 \leq [\text{Eu}/\text{Fe}] \leq +1.0$ and $[\text{Ba}/\text{Eu}] < 0.0$) and *r*-II ($[\text{Eu}/\text{Fe}] > +1.0$ and $[\text{Ba}/\text{Eu}] < 0.0$) stars, respectively (Beers & Christlieb 2005; Frebel 2018). Until recently, only ~ 25 *r*-II stars had been identified after their recognition some 25 years ago (Snedden et al. 1994, 1996). Characterization of additional examples of such stars is crucial in order to explore the origin of the astrophysical *r*-process, to constrain the nature of their likely progenitor(s) (e.g., neutron star mergers, Abbott et al. 2017; Drout et al. 2017; Shappee et al. 2017), and to measure the abundances of the radioactive chronometers thorium and uranium, which are only presently available for a handful of stars.

The *R*-Process Alliance (RPA) was recently established to fulfill the need for further observational constraints on the astrophysical origin of the *r*-process. Its overall science goal is to support stellar archaeology and nuclear astrophysics by identifying as many *r*-process-enhanced metal-poor stars as possible, building a sample of ~ 125 stars belonging to the rare *r*-II class. The RPA is envisioned as a multi-stage, multi-year effort to provide observational, theoretical, and laboratory-based constraints on the nature and origin of the astrophysical *r*-process. Even at this early stage, this effort has already identified two *r*-II stars with detected thorium and uranium (Placco et al. 2017; Holmbeck et al. 2018), a bright *r*-II star at $[\text{Fe}/\text{H}] \sim -2$ (Sakari et al. 2018b), the first CEMP-*r* + *s* star (Gull et al. 2018), and a metal-poor star ($[\text{Fe}/\text{H}] = -1.47$) with an extreme *r*-process enhancement (Roederer et al. 2018). In addition, the RPA has generated four catalogs of stars of particular interest: one with candidates selected from medium-resolution spectroscopy from RAVE (RAial Velocity Experiment; Steinmetz et al. 2006; Kordopatis et al. 2013), published by Placco et al. (2018) and three with high-resolution spectroscopic follow-up observations (Ezzeddine et al. 2018, in preparation; Hansen et al. 2018; Sakari et al. 2018a). The present paper is the fifth RPA catalog.

The Best & Brightest Survey (B&B; Schlafman & Casey 2014) made use of the contrast in the mid-IR photometric bands from the *WISE* (*Wide-field Infrared Survey Explorer*; Wright et al. 2010) satellite mission to ground-based optical and near-IR photometry to select over 11,000 candidate VMP and EMP stars, with an overall success rate of 30% (VMP) and $\sim 5\%$ (EMP), which is competitive with previous surveys (see, e.g., Schörck et al. 2009; Youakim et al. 2017). High-resolution spectroscopic follow-up of selected candidates successfully identified some of the first metal-poor stars in the inner Galaxy (Casey & Schlafman 2015) and also the most neutron-capture poor star ever observed (Casey & Schlafman 2017). The B&B survey has the advantage that all of their candidates are brighter than $V = 14.0$, where many other surveys saturate. By obtaining medium-resolution spectroscopy of B&B candidates, we have the opportunity to assemble a definitive sample of relatively bright CEMP and non-CEMP stars at low metallicity, enabling studies of the known subclasses of CEMP stars (CEMP-*s*, CEMP-*r*, CEMP-*i*,

CEMP-no), as well as to identify *r*-I and *r*-II candidates, both of which are ideal for future high-resolution spectroscopic observations from the ground and in space (see, e.g., Roederer et al. 2012a, 2012b, 2014; Placco et al. 2014a, 2015a; Roederer et al. 2016).

This paper reports on the medium-resolution ($R \sim 1200\text{--}2000$) spectroscopic follow-up of low-metallicity star candidates selected from the B&B survey. The main goal is to determine atmospheric parameters and carbon abundances for a large sample of stars, which will be used as criteria for targeted high-resolution spectroscopic follow-ups, including the RPA. This paper is outlined as follows: Section 2 describes the medium-resolution spectroscopic observations, followed by the estimates of the stellar atmospheric parameters and abundances in Section 3. We describe the main abundance trends of our targets, based on $[\text{C}/\text{Fe}]$ and $[\alpha/\text{Fe}]$, in Section 4, and compare our stellar parameter determinations with results obtained from high-resolution spectroscopic observations by the RPA in Section 5. Our conclusions and prospects for future work are provided in Section 6.

2. Target Selection and Observations

The medium-resolution spectroscopic follow-up campaign was conducted from semesters 2015B to 2017A, and collected spectra of 857 unique metal-poor candidates. Below we describe the target selection from the B&B database and the subsequent observations.

2.1. Target Selection from the B&B Database

The candidates for the spectroscopic follow-up were selected from two different versions of the B&B database, $v1$ and $v2$, the latter having an improved selection criteria. Observations conducted in semester 2015B made use of $v1$, restricted in magnitude by $V > 13.2$ (in order to avoid conflict with a similar survey of brighter B&B stars we were already conducting). For semesters 2016A, 2016B, and 2017A, $v2$ was used, with the following restrictions:

- \star Magnitude: $12.5 < V < 13.2$,
- \star Proper motion: $0 < \mu_{\text{total}}^{18}$ (mas yr $^{-1}$) < 25 ,
- \star Reddening: $E(B - V) < 0.05$.

In total, 71 stars were observed from $v1$ and 786 from $v2$. Stars in the $V < 12.5$ mag range were observed by a different program and the restrictions in proper motion/reddening were designed to minimize contamination from the numerous foreground disk-like stars. The effectiveness of these criteria in the selection of metal-poor stars is further evaluated in Section 3 below.

Table 1 lists the object name, observation date, telescope, instrument, program ID, and exposure time for the observed candidates; Table 2 lists their coordinates, magnitudes, color indices, and reddening estimates from the dust maps of Schlafly & Finkbeiner (2011). *J* and *K* magnitudes (with photometric quality flags) were retrieved from the Two Micron All Sky Survey (2MASS; Skrutskie et al. 2006), while *B* and *V* magnitudes from the AAVSO Photometric All-Sky Survey (APASS; Henden & Munari 2014). The upper panels of Figure 1 show the Galactic (left) and equatorial (right)

¹⁸ $\mu_{\text{total}} = \sqrt{\mu_{\text{R.A.}}^2 + \mu_{\text{decl.}}^2}$. Proper motions retrieved from the fourth US Naval Observatory CCD Astrograph Catalog (UCAC4; Zacharias et al. 2013).

Table 1
Observing Details

Star Name (2MASS)	Date (UTC)	Telescope	Instrument	Proposal ID	Exp. (s)
J000045.79+380245.7	2015 Nov 8	Gemini-North	GMOS-N	GN-2015B-Q-100	300
J000106.55+452812.5	2015 Nov 8	Gemini-North	GMOS-N	GN-2015B-Q-100	300
J000111.95+032105.0	2017 Jul 7	Mayall	KOSMOS	17A-0295	600
J000123.03+495329.1	2015 Nov 11	Gemini-North	GMOS-N	GN-2015B-Q-100	370
J000137.83+500539.6	2015 Nov 16	Gemini-North	GMOS-N	GN-2015B-Q-100	600
J000212.23–224138.9	2015 Nov 9	Gemini-South	GMOS-S	GS-2015B-Q-104	600
J000216.68–245349.5	2015 Nov 9	Gemini-South	GMOS-S	GS-2015B-Q-104	600
J000312.65–001504.4	2015 Nov 24	Gemini-South	GMOS-S	GS-2015B-Q-104	600
J000438.51–631242.6	2015 Nov 23	Gemini-South	GMOS-S	GS-2015B-Q-104	600
J000530.64+002210.7	2015 Dec 9	Gemini-South	GMOS-S	GS-2015B-Q-104	600

(This table is available in its entirety in machine-readable form.)

Table 2
Coordinates, Magnitudes, Color Indices, and Reddening Estimates

Star Name (2MASS)	α (J2000)	δ (J2000)	l (deg)	b (deg)	V (mag)	$(B - V)$	J (mag)	$(J - K)$	ph_qual ^a	$E(B - V)$
J000045.79+380245.7	00:00:45.84	+38:02:45.6	112.055	−23.753	13.883	0.958	11.903	0.657	AAA	0.089
J000106.55+452812.5	00:01:06.48	+45:28:12.0	113.764	−16.504	13.348	1.042	11.317	0.722	AAA	0.118
J000111.95+032105.0	00:01:12.00	+03:21:03.6	99.309	−57.198	12.803	0.809	11.049	0.620	AAA	0.021
J000123.03+495329.1	00:01:23.04	+49:53:27.6	114.722	−12.181	13.693	0.929	11.995	0.631	AAA	0.116
J000137.83+500539.6	00:01:37.92	+50:05:38.4	114.802	−11.990	13.803	0.916	11.993	0.666	AAA	0.118
J000212.23–224138.9	00:02:12.24	−22:41:38.4	51.912	−77.996	13.273	0.758	11.727	0.564	AAA	0.018
J000216.68–245349.5	00:02:16.80	−24:53:49.2	41.605	−78.737	13.478	0.841	11.841	0.595	AAA	0.016
J000312.65–001504.4	00:03:12.72	−00:15:03.6	97.639	−60.733	13.641	1.148	11.298	0.754	AAA	0.029
J000438.51–631242.6	00:04:38.40	−63:12:43.2	311.689	−53.113	13.477	0.960	11.605	0.643	AAA	0.016
J000530.64+002210.7	00:05:30.72	+00:22:12.0	99.192	−60.368	13.740	0.939	11.749	0.655	AAA	0.055

Note.^a 2MASS JHK photometric quality flag. Further details are given at <http://vizier.u-strasbg.fr/viz-bin/VizieR-n?-source=METAnot&catid=2246¬id=5>.

(This table is available in its entirety in machine-readable form.)

coordinates of the observed targets and the lower panels show the distribution of their extinction-corrected V_0 magnitudes (left) and dereddened $(B - V)_0$ color indices (right). Also shown are the stripe-density profiles and the average values. By design, this sample consists of mostly bright ($V < 13.2$) and cool ($T_{\text{eff}} < 5500$ K) low-metallicity candidates, which are ideal for the high-resolution spectroscopic follow-up program being executed by the RPA.

2.2. Medium-resolution Follow-up Observations

Spectroscopic data were gathered using five telescope/instrument setups: (i) SOAR/Goodman, (ii) Gemini North/GMOS-N, (iii) Gemini South/GMOS-S, (iv) Mayall/KOSMOS, and (v) NTT/EFOSC-2. For consistency across the different instruments, we chose grating/slit combinations that would yield a resolving power $R \sim 1200$ – 2000 , and exposure times sufficient to reach a signal-to-noise ratio of at least $S/N \sim 30$ per pixel at the Ca II K line (3933.3 Å). Calibration frames included arc-lamp exposures, bias frames, and quartz flats. All tasks related to spectral reduction, extraction, and wavelength calibration were performed using standard IRAF¹⁹ packages.

Figure 2 shows the spectra for 50 stars (randomly selected from the 857 star database) followed-up in this work, color-coded by the different telescopes used for the observations. The shaded areas highlight wavelength regions of interest for atmospheric parameter and abundance determinations (see Section 3 for details). Even though there are noticeable differences in coverage, CCD response, and resolution, these spectra are all within acceptable ranges for the analysis performed in this work. Details on each observing setup are provided below.

Gemini North and South Telescopes—474 stars were observed with the twin 8.1 m Gemini North (134 stars) and Gemini South (340 stars) telescopes and the GMOS (Gemini Multi-Object Spectrographs; Davies et al. 1997; Gimeno et al. 2016) instruments. In both cases, we used the B600 1 mm^{-1} grating (G5323 for GMOS South and G5307 for GMOS North) and a $1''$ slit, resulting in a wavelength coverage in the range [3200:5800] Å at resolving power $R \sim 2000$.

ESO New Technology Telescope—256 stars were observed with the 3.58 m New Technology Telescope (NTT), located at La Silla Observatory, part of the European Southern Observatory. We used the EFOSC-2 (ESO Faint Object Spectrograph and Camera v.2; Buzzoni et al. 1984) instrument with Grism#7 (600 gr mm^{-1}) and a $1''$ slit, resulting in a

¹⁹ <http://iraf.noao.edu>

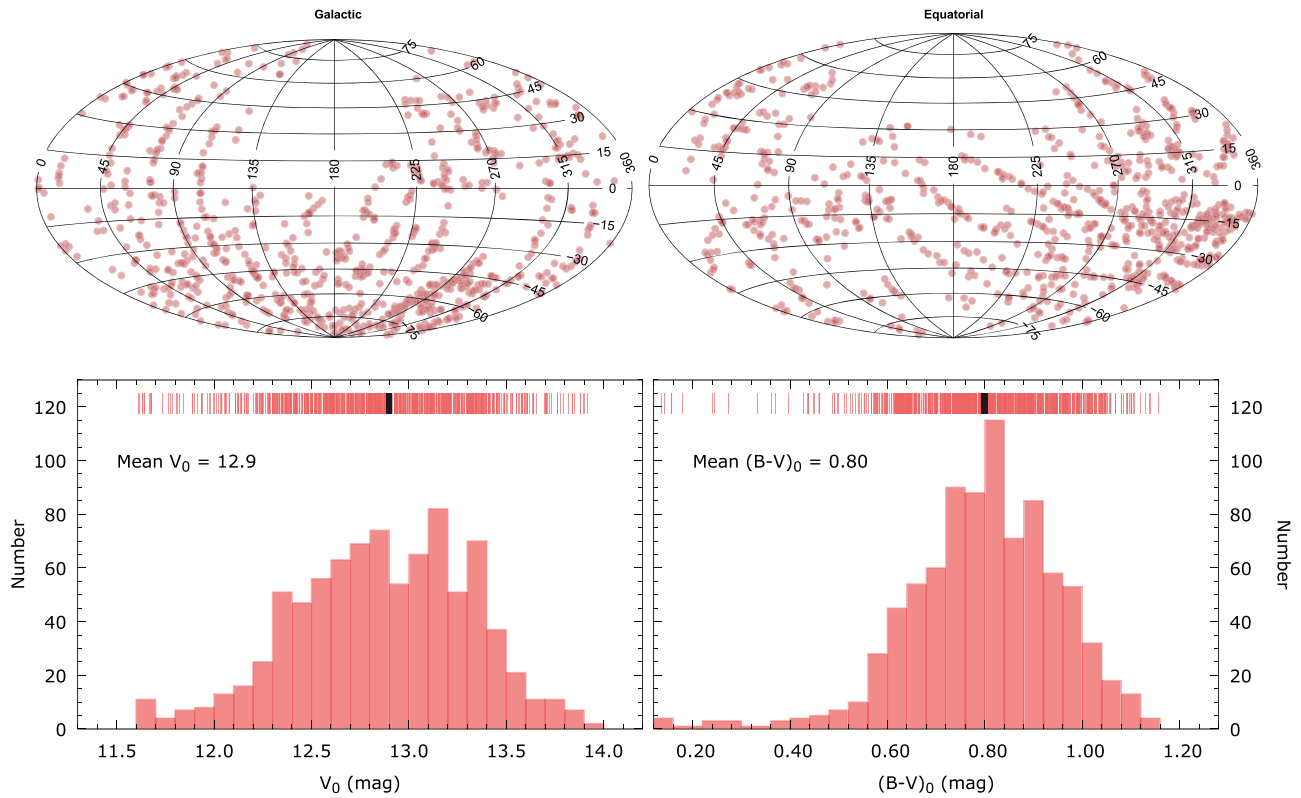


Figure 1. Upper panels: galactic and equatorial coordinates for the observed targets. Lower panels: distributions of absorption-corrected V_0 magnitudes and dereddened $(B - V)_0$ colors. Stripe-density profiles are shown above the histograms, with the average value highlighted in black.

wavelength coverage in the range $[3300:5100] \text{ \AA}$ at resolving power $R \sim 1200$.

KPNO Mayall Telescope—73 stars were observed with the 4 m Mayall telescope, located at Kitt Peak National Observatory, using the KOSMOS (Kitt Peak Ohio State Multi-Object Spectrograph; Martini et al. 2014) instrument. We used the 600 l mm^{-1} grating, the blue setting, and a $0''.9$ slit, resulting in a wavelength coverage in the range $[3600:6300] \text{ \AA}$ at resolving power $R \sim 1800$.

SOAR Telescope—54 stars were observed with the 4.1 m Southern Astrophysical Research (SOAR) telescope. The Goodman Spectrograph (Clemens et al. 2004) was used with the 600 l mm^{-1} grating, the blue setting, and a $1''.0$ slit, resulting in a wavelength coverage in the range $[3600:6200] \text{ \AA}$ at resolving power $R \sim 1500$.

3. Stellar Parameters and Abundances

Stellar atmospheric parameters (T_{eff} , $\log g$, and $[\text{Fe}/\text{H}]$), as well as carbonicity ($[\text{C}/\text{Fe}]$) and α -to-iron ratios ($[\alpha/\text{Fe}]$), were determined using the n-SSPP (Beers et al. 2014, 2017), a modified version of the SEGUE Stellar Parameter Pipeline (SSPP; Lee et al. 2008a, 2008b, 2011, 2013). The n-SSPP uses as input the observed spectrum and photometric information for a given object. There are several internal routines that calculate the atmospheric parameters based on spectral line indices, photometric calibrations, and matching with a database of synthetic spectra. The $[\text{C}/\text{Fe}]$ and $[\alpha/\text{Fe}]$ are estimated from the strength of the CH G -band molecular feature at $\sim 4300 \text{ \AA}$ and the Mg I triplet at $5150\text{--}5200 \text{ \AA}$, respectively. Details on

the n-SSPP processing for spectra similar to the ones analyzed in this work can be found in Placco et al. (2018).

Figure 3 shows, in the left column of panels, the effect of changes in metallicity on the Ca II spectral lines for stars with similar T_{eff} , and increasing $[\text{Fe}/\text{H}]$ (from $[\text{Fe}/\text{H}] = -3.25$ to $[\text{Fe}/\text{H}] = -0.36$). Listed for each spectra are NAME/ $T_{\text{eff}}/\log g/[\text{Fe}/\text{H}]/[\text{C}/\text{Fe}]$. At this resolving power, the Ca II K line is the main proxy for metallicity in the optical wavelength regime. The right column of panels in Figure 3 shows spectra with increasing T_{eff} (from $T_{\text{eff}} = 4549 \text{ K}$ to $T_{\text{eff}} = 8985 \text{ K}$) and its effect on the strength of three hydrogen Balmer lines.

The n-SSPP was able to estimate T_{eff} and $\log g$ for 842 out of the 857 stars observed. The 15 stars without adopted parameters had low S/N spectra and/or large mismatches between the color-based temperatures and the spectroscopic calibrations. Metallicities were determined for $\sim 93\%$ of the observed sample (796 stars). The nondeterminations arise from a lack of temperature estimates by the n-SSPP, or stars with core emission in the Ca II K line. The $[\text{C}/\text{Fe}]$ and $[\alpha/\text{Fe}]$ abundance ratios were estimated for 793 and 584 stars, respectively. The carbon-abundance determination is not carried out for low-quality spectra (mostly $\text{S/N} < 10$), or in spectra where the CH G -band molecular feature is too weak to be reliably distinguished from the underlying noise (usually for $T_{\text{eff}} > 6500 \text{ K}$; see Placco et al. 2016a). In addition, due to the lack of spectral coverage, $[\alpha/\text{Fe}]$ was not obtained for the NTT/EFOSC-2 spectra. Final atmospheric parameters and abundances for the sample are listed in Table 3. Also included in the table are the corrections for carbon abundances, based on

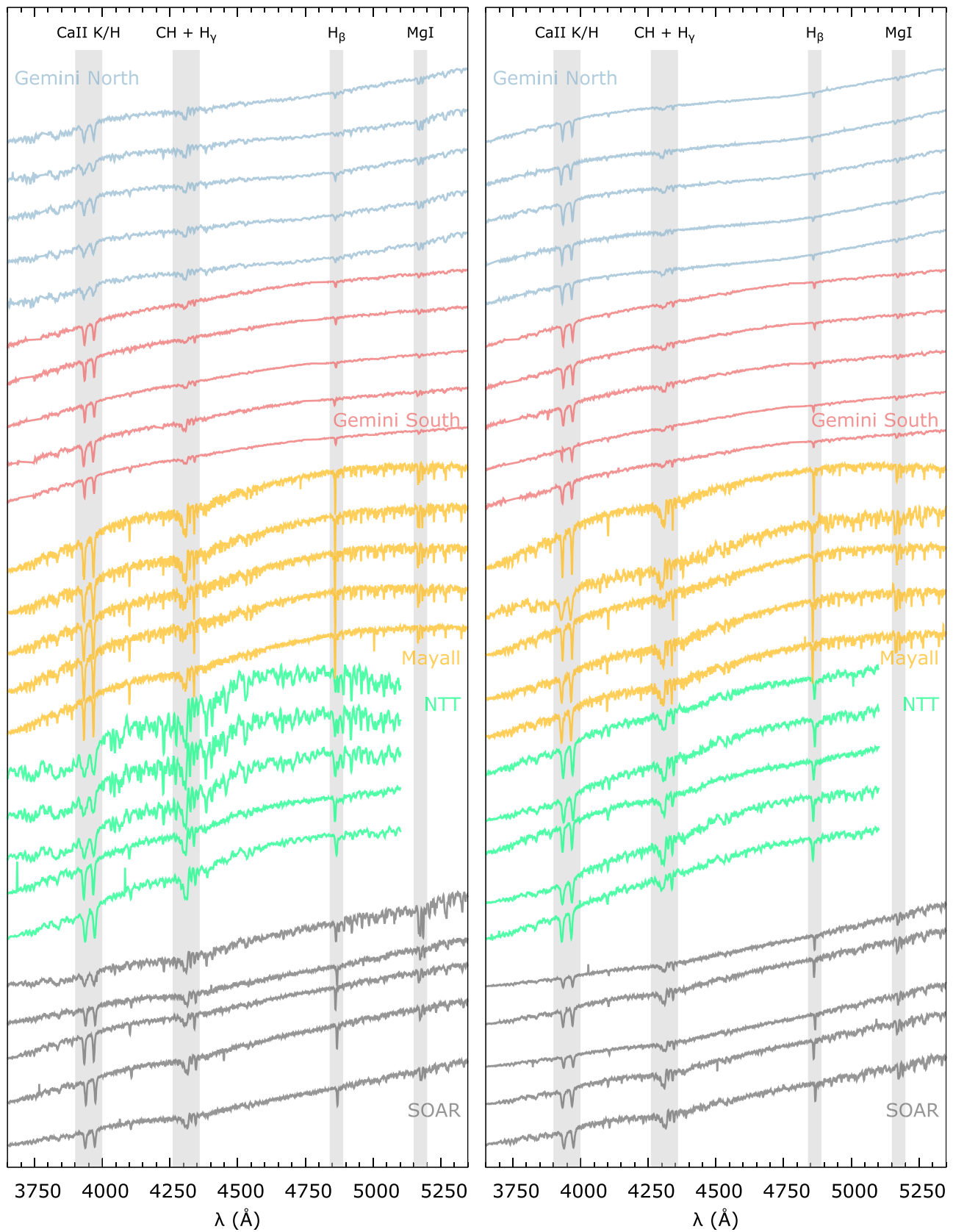


Figure 2. Example spectra for 50 (randomly selected) program stars. The colors represent the five different telescopes used for the observations. The shaded areas highlight regions of interest (Ca II, CH G-band+H γ , H β , and Mg I, respectively).

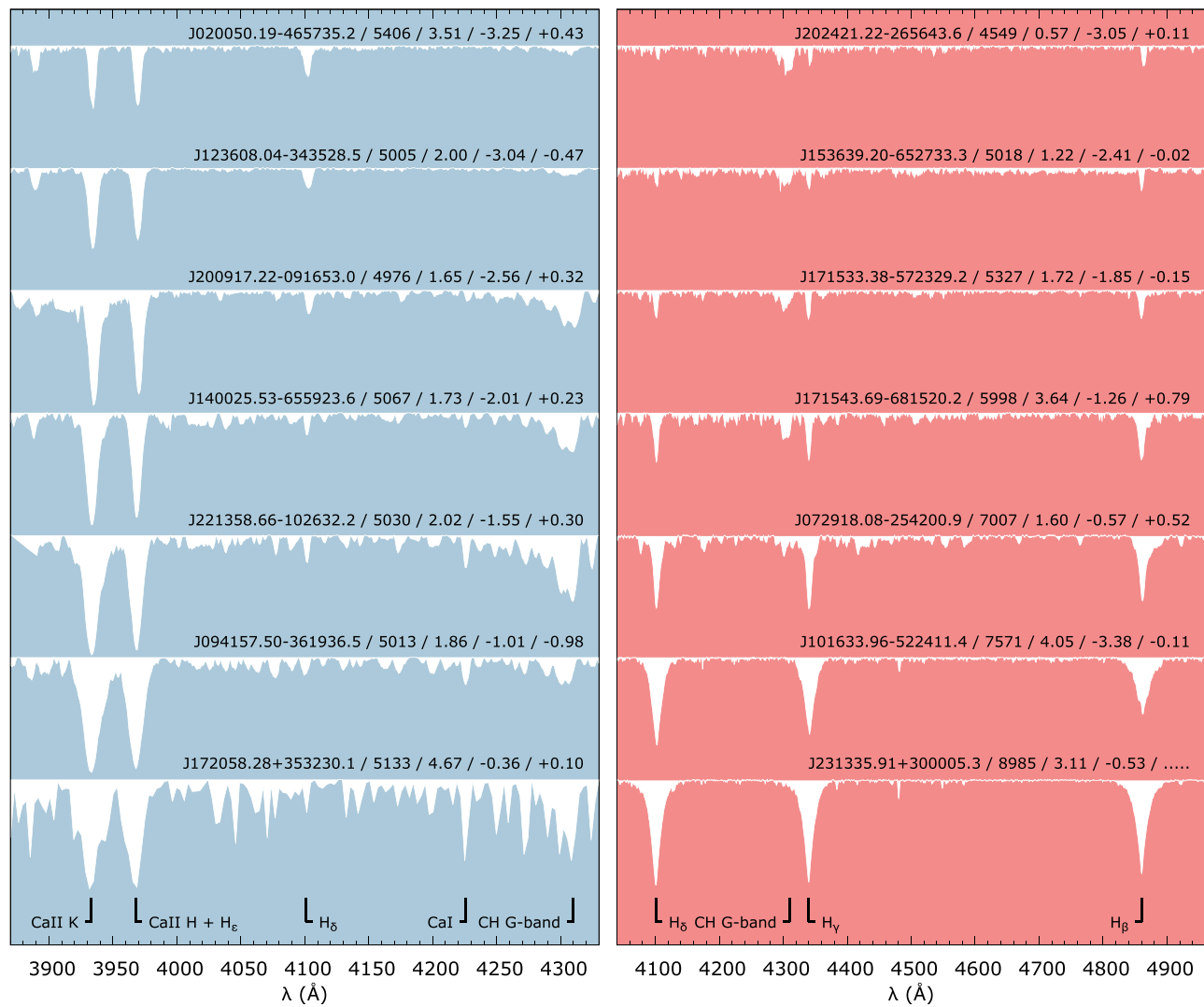


Figure 3. Left panel: observed spectra with similar temperatures, showing the effect of increasing metallicities on the strength of the Ca II absorption features. Right panel: effect of increasing temperatures on the hydrogen Balmer absorption features. Listed for each spectrum are NAME/ T_{eff} / $\log g$ / $[\text{Fe}/\text{H}]$ / $[\text{C}/\text{Fe}]$.

Table 3
Stellar Parameters and Abundances from the n-SSPP

Star Name (2MASS)	T_{eff} (K)	$\log g$ (cgs)	$[\text{Fe}/\text{H}]$	$[\text{C}/\text{Fe}]$	$\Delta[\text{C}/\text{Fe}]^{\text{a}}$	$[\text{C}/\text{Fe}]_{\text{cor}}^{\text{b}}$	$A(\text{C})_{\text{cor}}^{\text{c}}$	$[\alpha/\text{Fe}]$
J000045.79+380245.7	4748	2.97	-0.35	-0.59	+0.03	-0.56	+7.52	+0.03
J000106.55+452812.5
J000111.95+032105.0	4984	1.89	-2.05	+0.14	+0.13	+0.27	+6.65	+0.22
J000123.03+495329.1	5280	3.93	-0.69	+0.30	0.00	+0.30	+8.04	+0.26
J000137.83+500539.6	4902	3.20	-0.47	-0.25	+0.02	-0.23	+7.74	+0.13
J000212.23-224138.9	5209	2.30	-2.52	+0.68	+0.01	+0.69	+6.61	-0.05
J000216.68-245349.5	5018	1.75	-2.32	-0.06	+0.29	+0.23	+6.34	+0.42
J000312.65-001504.4	4461	3.36
J000438.51-631242.6	5086	4.19	-0.61	+0.48	0.00	+0.48	+8.30	-0.17
J000530.64+002210.7	4921	2.73	-0.25	-0.71	+0.03	-0.68	+7.50	+0.07

Notes.

^a Carbon correction from Placco et al. (2014b).

^b Corrected carbon-to-iron ratio.

^c Corrected absolute carbon abundance.

(This table is available in its entirety in machine-readable form.)

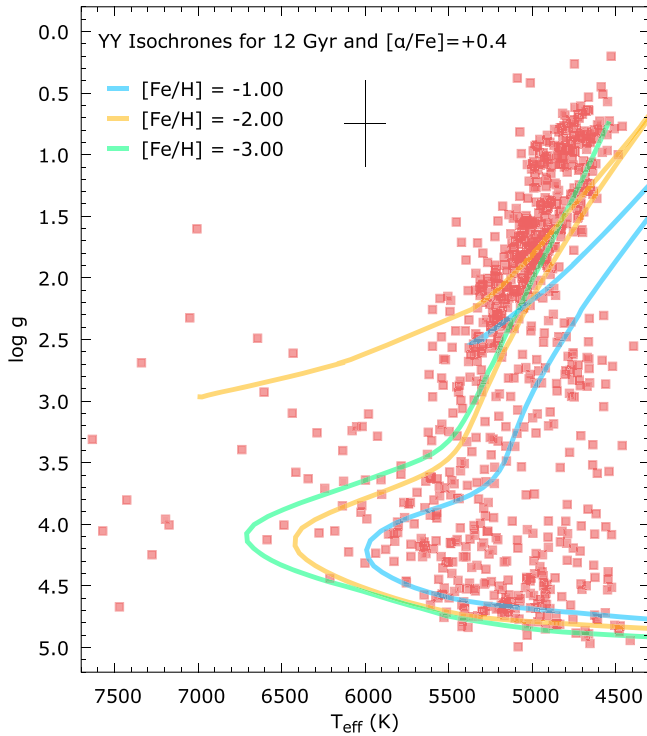


Figure 4. Surface gravity vs. T_{eff} (H-R) diagram for the program stars, using the parameters calculated by the n-SSPP, listed in Table 3. Overplotted are the YY Isochrones (12 Gyr, $0.8 M_{\odot}$, $[\alpha/\text{Fe}] = +0.4$; Demarque et al. 2004) for $[\text{Fe}/\text{H}] = -2.0$, -2.5 , and -3.0 , and horizontal-branch tracks from Dotter et al. (2008).

the stellar-evolution models presented in Placco et al. (2014b), the final $[\text{C}/\text{Fe}]$, and $A(\text{C})$,²⁰ the latter two including the corrections.

With the calculated metallicities, we were able to test the effectiveness of the proper motion and reddening cuts described in Section 2. From the $\nu 1$ database, for which no extra proper motion and reddening cuts were applied, 48% of the observed targets have $[\text{Fe}/\text{H}] \leq -1.0$ and 9% have $[\text{Fe}/\text{H}] \leq -2.0$. These numbers increase to 71% for $[\text{Fe}/\text{H}] \leq -1.0$ and 42% for $[\text{Fe}/\text{H}] \leq -2.0$, when observing candidates selected from the $\nu 2$ database, with the cuts applied. By combining both subsamples, 69% of the stars have $[\text{Fe}/\text{H}] \leq -1.0$, 39% have $[\text{Fe}/\text{H}] \leq -2.0$, and 2% have $[\text{Fe}/\text{H}] \leq -3.0$. These fractions are somewhat smaller than the values reported by Placco et al. (2018) for the follow-up of RAVE low-metallicity candidates. However, the RAVE stars already had preliminary $[\text{Fe}/\text{H}]$ estimates from their moderate-resolution spectra, while the B&B star candidates were originally selected based on photometry alone.

The distribution of effective temperatures and surface gravities derived for the B&B follow-up sample is shown in Figure 4. Solid lines represent the Yale–Yonsei Isochrones (12 Gyr, $0.8 M_{\odot}$, $[\alpha/\text{Fe}] = +0.4$; Demarque et al. 2004) for $[\text{Fe}/\text{H}] = -2.0$, -2.5 , and -3.0 . Also shown are the Horizontal-Branch tracks from the Dartmouth Stellar Evolution Database (Dotter et al. 2008), for the same input parameters. Since the B&B is a magnitude-limited survey, and further

brightness constraints were applied before observations, it is expected that the present sample would be dominated by stars in the subgiant and giant evolutionary stages. There is a noticeable shift of about $+150$ K between the data and the isochrones. The same offset is seen in the RAVE stars followed-up in Placco et al. (2018), even though the T_{eff} values for that sample agree well with estimates based on the infrared flux method of Casagrande et al. (2010). Comparison with parameters determined from high-resolution spectroscopy within the RPA will help address these differences. Further details are provided in Section 5. Typical uncertainties for the atmospheric parameters calculated by the n-SSPP are 125 K for T_{eff} , 0.35 dex for $\log g$, and 0.15–0.20 dex for $[\text{Fe}/\text{H}]$, $[\text{C}/\text{Fe}]$, and $[\alpha/\text{Fe}]$.

4. Carbonicity and α -to-iron Abundance Ratios

The carbonicity and α -to-iron ratios estimated by the n-SSPP can provide useful constraints on the formation scenarios for metal-poor stars, and also serve as criteria to assemble lists for high-resolution spectroscopic follow-up. Figure 5 shows the distribution of the carbon abundances ($A(\text{C})$, as corrected—left side) and the α -element abundance ratios (right side), as a function of the $[\text{Fe}/\text{H}]$ estimated in this work. The lower and side panels show marginal distributions for each quantity. There is no significant trend for the $[\alpha/\text{Fe}]$ ratios, with values ranging from -0.2 to $+0.6$. These are within expectation for samples with similar $[\text{Fe}/\text{H}]$ ranges and Galactic chemical evolution models (Reggiani et al. 2017).

The $A(\text{C})$ versus $[\text{Fe}/\text{H}]$ diagram provides an important diagnostic for the type(s) of progenitor(s) that could have formed a given star (Spite et al. 2013; Bonifacio et al. 2015; Hansen et al. 2015; Yoon et al. 2016). Yoon et al. (2016) proposed a classification of CEMP stars, based on $A(\text{C})$ versus $[\text{Fe}/\text{H}]$ (both of which can be estimated using medium-resolution spectra alone), into three groups, the so-called Yoon–Beers diagram. Using the criteria described in Placco et al. (2018), shown in Figure 5, we find 97 stars in Group I and 36 stars in Group II, with no stars belonging to Group III. The stars in Group II, which are likely to be CEMP-no ($[\text{C}/\text{Fe}] \geq +0.7$ and $[\text{Ba}/\text{Fe}] < 0.0$), are ideal targets for high-resolution spectroscopic follow-up and determination of their light-element chemical abundance patterns, as such stars provide precious information about nucleosynthesis pathways in the early universe.

Since the original B&B sample did not have any indicators of carbon enhancement, one would expect that the CEMP fractions for the stars observed in this work are similar to values from the literature for other “carbon-blind” samples. The lower left panel of Figure 5 shows the CEMP fractions (using the corrected $[\text{C}/\text{Fe}]$, values—see Section 3 for further details) for metallicities in the range $[-3.0, -1.0]$. There is an overall good agreement (within 1σ) with the values from Placco et al. (2018). The fraction found for $[\text{Fe}/\text{H}] < -2.5$ in this work ($31^{+9}_{-7}\%$)²¹ agrees very well with the fraction found in Schlafman & Casey (2014) for the same metallicity range, $28^{+18}_{-13}\%$. There is also a good agreement for the fractions at $[\text{Fe}/\text{H}] \leq -2.0$ and -3.0 from this work ($22^{+5}_{-4}\%$ and $47^{+22}_{-21}\%$,

²⁰ $A(\text{C}) = \log(N_{\text{C}}/N_{\text{H}}) + 12$.

²¹ Uncertainties in the fractions are represented by the Wilson score confidence intervals (Wilson 1927).

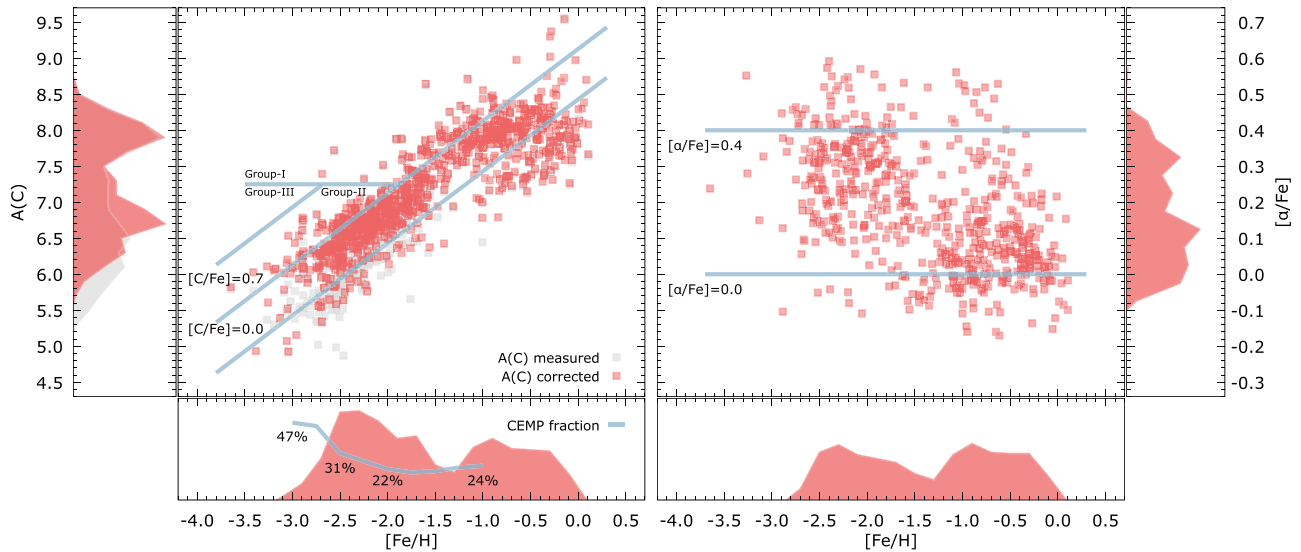


Figure 5. Absolute carbon, $A(C)$, corrected as described in the text—left panel), and α -element abundance ratios, $[\alpha/Fe]$ (right panel), as a function of the metallicity calculated by the n-SSPP. The side and lower panels show the marginal distributions for each quantity. The solid line in the lower panel shows the cumulative CEMP fractions for the stars with $-3.0 \leq [Fe/H] \leq -1.0$.

respectively) and the fractions calculated using abundances from high-resolution spectroscopy (20% and 43%; Placco et al. 2014b).

5. Comparison with High-resolution Spectroscopic Data from the RPA

In this section we present a comparison between the atmospheric parameters estimated in this work and values²² from the RPA high-resolution data release papers (Hansen et al. 2018; Sakari et al. 2018a). We combine the medium-resolution spectra from this work with data from Placco et al. (2018), which are of similar resolution, and were also processed by the n-SSPP. In total, 218 stars were used for these comparisons; results are presented in Figure 6. The left column of panels shows the differences between the parameters determined by the n-SSPP, $T_{\text{eff n-SSPP}}$, $\log g_{\text{n-SSPP}}$, and $[Fe/H]_{\text{n-SSPP}}$, and the values from high-resolution, $T_{\text{eff HIGH}}$, $\log g_{\text{HIGH}}$, and $[Fe/H]_{\text{HIGH}}$, as a function of the high-resolution spectroscopic values. The horizontal solid line is the average of the residuals, while the darker and lighter shaded areas represent the 1σ and 2σ regions, respectively. Also shown are locally weighted regression (*loess*) lines. The right column of panels shows histograms of the residuals between the n-SSPP and high-resolution parameters. Each panel also lists the average and standard deviation of the residual distribution.

Inspection of Figure 6, in particular, the *loess* lines, reveals that there are no relevant trends in the comparisons other than constant shifts (values from this work minus parameters from the RPA) for T_{eff} (152 K), $\log g$ (0.10 dex), and $[Fe/H]$ (−0.2 dex). In addition, the standard deviations of the residuals (168 K for T_{eff} , 0.5 dex for $\log g$, and 0.3 dex for $[Fe/H]$), are within the expected values for such comparisons (e.g., Lee et al. 2013; Beers et al. 2014). It is worth noting that the shifts T_{eff} and $[Fe/H]$ are not independent, because changes in temperature affect the strength of the absorption features in the

stellar atmospheres. Further analyses and corrections for the medium-resolution parameters will be conducted once the first phase of “snapshot” (moderate S/N, moderately high-resolution) observations of the RPA are finished, which should yield a database of at least 2000 stars with high-resolution determinations for comparison.

6. Conclusions

We have presented results from a medium-resolution ($R \sim 1200\text{--}2000$) spectroscopic follow-up of low-metallicity star candidates selected from the Best & Brightest Survey. Our observing campaign ran from semesters 2015B to 2017A, and used five different telescope/instrument configurations, in both the southern and northern hemispheres. Atmospheric parameters and abundances for carbon and the α -elements were calculated using our well-tested n-SSPP pipeline. From the 857 unique stars observed, 553 were confirmed to be metal-poor ($[Fe/H] \leq -1.0$), and 133 were carbon-enhanced ($[C/Fe] \geq +0.7$), after evolutionary corrections have been applied. There are 36 CEMP Group II stars that are currently being followed-up in high-resolution, to determine their chemical abundance patterns, and compare with yields from theoretical models of Population III stellar nucleosynthesis. We also showed that the success rate for the identification of very low-metallicity stars can be significantly increased (from 9%, to 42%, for $[Fe/H] \leq -2.0$), when proper motions are also used as a selection criteria, primarily due to the exclusion of foreground disk-like stars.

Comparisons between the parameters determined in this work and values from the RPA catalogs reveal that the residual zero-point offsets are within 1σ for T_{eff} , (152 K), $\log g$, (0.10 dex), and $[Fe/H]$, (−0.2 dex), which allow for a successful target selection for high-resolution spectroscopic follow-up. The catalog generated by this work will continue to serve as a reliable source of targets for the RPA and other projects in the future.

²² For this comparison we used the parameters calculated assuming local thermodynamic equilibrium.

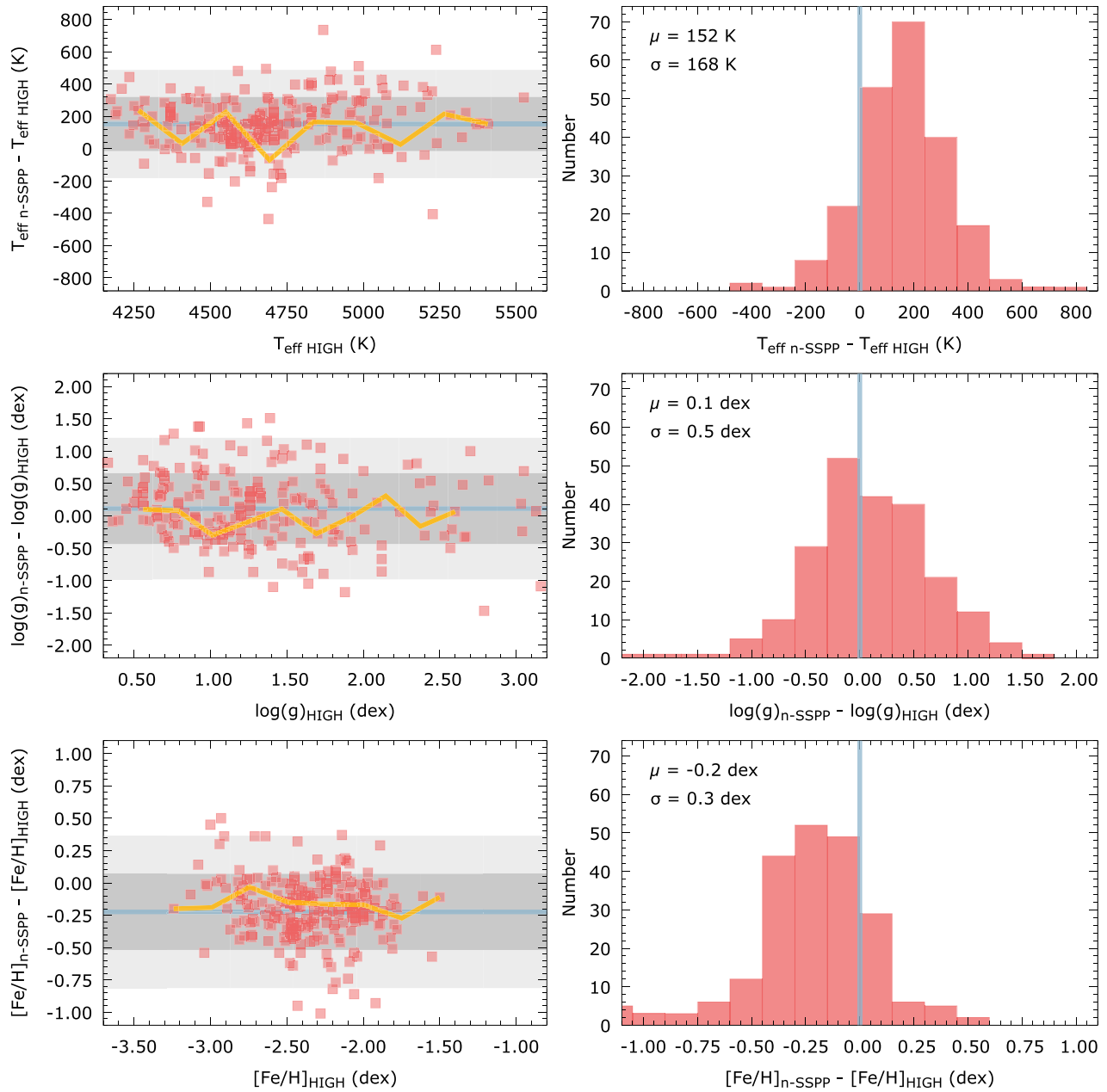


Figure 6. Left panels: differences between the parameters determined by the n-SSPP, $T_{\text{eff n-SSPP}}$, $\log g_{\text{n-SSPP}}$, and $[\text{Fe}/\text{H}]_{\text{n-SSPP}}$, and the values from high-resolution, $T_{\text{eff HIGH}}$, $\log g_{\text{HIGH}}$, and $[\text{Fe}/\text{H}]_{\text{HIGH}}$, as a function of the high-resolution spectroscopic values. The horizontal solid line is the average of the residuals, while the darker and lighter shaded areas represent the 1σ and 2σ regions, respectively. Also shown are locally weighted regression (*loess*) lines. Right panels: histograms of the residuals between the n-SSPP and high-resolution parameters shown in the left panels. Each panel also lists the average and σ of the residual distribution.

We thank Kevin C. Schlafman and Andrew R. Casey for kindly providing early access to the candidate lists from the Best & Brightest Survey. The authors acknowledge partial support for this work from grant PHY 1430152; Physics Frontier Center/JINA Center for the Evolution of the Elements (JINA-CEE), awarded by the US National Science Foundation (NSF). J.C. acknowledges support from CONICYT project Basal AFB-170002 and by the Chilean Ministry for the Economy, Development, and Tourism's Programa Iniciativa Científica Milenio grant IC 120009, awarded to the Millennium Institute of Astrophysics. S.R. acknowledges partial financial support from FAPESP and CNPq. This study was financed in part by the Coordenação de Aperfeiçoamento de Pessoal de Nível Superior

—Brasil (CAPES)—Finance Code 001. Y.S.L. acknowledges support from the National Research Foundation (NFR) of Korea grant funded by the Ministry of Science and ICT (No.2017R1A5A1070354 and NRF-2018R1A2B6003961). E.S. and K.Y. gratefully acknowledge funding by the Emmy Noether program from the Deutsche Forschungsgemeinschaft (DFG). A. P.J. is supported by NASA through Hubble Fellowship grant *HST*-HF2-51393.001 awarded by the Space Telescope Science Institute, which is operated by the Association of Universities for Research in Astronomy, Inc., for NASA, under contract NAS5-26555. I.U.R. acknowledges support from NSF grants AST 1613536 and AST 1815403. Based on observations at Kitt Peak National Observatory, National Optical Astronomy Observatory

(NOAO Prop. ID: 17A-0295), which is operated by the Association of Universities for Research in Astronomy (AURA) under cooperative agreement with the National Science Foundation. The authors are honored to be permitted to conduct astronomical research on Iolkam Du'ag (Kitt Peak), a mountain with particular significance to the Tohono O'odham. Based on observations obtained at the Gemini Observatory (Prop. IDs: GN-2015B-Q-100, GN-2016B-Q-85, GS-2015B-Q-104, GS-2016A-Q-107, GS-2016B-Q-86), which is operated by the Association of Universities for Research in Astronomy, Inc., under a cooperative agreement with the NSF on behalf of the Gemini partnership: the National Science Foundation (United States), the National Research Council (Canada), CONICYT (Chile), Ministerio de Ciencia, Tecnología e Innovación Productiva (Argentina), and Ministério da Ciência, Tecnologia e Inovação (Brazil). Based on observations obtained at the Southern Astrophysical Research (SOAR) telescope (Prop. ID: 2017A-0016), which is a joint project of the Ministério da Ciência, Tecnologia, e Inovação (MCTI) da República Federativa do Brasil, the U.S. National Optical Astronomy Observatory (NOAO), the University of North Carolina at Chapel Hill (UNC), and Michigan State University (MSU). Based on observations collected at the European Organisation for Astronomical Research in the Southern Hemisphere under ESO programme(s) 097.D-0196(A), 097.D-0196(B), 098.B-0618(A), 098.D-0434(A), and 099.D-0428(A). This research was made possible through the use of the AAVSO Photometric All-Sky Survey (APASS), funded by the Robert Martin Ayers Sciences Fund. This publication makes use of data products from the Two Micron All Sky Survey, which is a joint project of the University of Massachusetts and the Infrared Processing and Analysis Center/California Institute of Technology, funded by the National Aeronautics and Space Administration and the National Science Foundation. This research has made use of NASA's Astrophysics Data System Bibliographic Services; the arXiv pre-print server operated by Cornell University; the SIMBAD database hosted by the Strasbourg Astronomical Data Center; and the online Q&A platform [stackoverflow](http://stackoverflow.com/) (<http://stackoverflow.com/>).

Software: `astrolibR` (Chakraborty et al. 2014), `AitoffR` (Rocha-Pinto 2014), `awk` (Aho et al. 1987), `gnuplot` (Williams & Kelley 2015), `IRAF` (Tody 1986, 1993), `n-SSPP` (Beers et al. 2014), `R-project` (R Core Team 2015), `sed` (McMahon 1974).

ORCID iDs

Vinicius M. Placco  <https://orcid.org/0000-0003-4479-1265>
 Rafael M. Santucci  <https://orcid.org/0000-0002-7529-1442>
 Timothy C. Beers  <https://orcid.org/0000-0003-4573-6233>
 Young Sun Lee  <https://orcid.org/0000-0001-5297-4518>
 Rana Ezzeddine  <https://orcid.org/0000-0002-8504-8470>
 Anna Frebel  <https://orcid.org/0000-0002-2139-7145>
 Terese T. Hansen  <https://orcid.org/0000-0001-6154-8983>
 Erika M. Holmbeck  <https://orcid.org/0000-0002-5463-6800>
 Alexander P. Ji  <https://orcid.org/0000-0002-4863-8842>
 Ian U. Roederer  <https://orcid.org/0000-0001-5107-8930>
 Charli M. Sakari  <https://orcid.org/0000-0002-5095-4000>

References

Abbott, B. P., Abbott, R., Abbott, T. D., et al. 2017, *ApJL*, 848, L12
 Aho, A. V., Kernighan, B. W., & Weinberger, P. J. 1987, *The AWK Programming Language* (Boston, MA: Addison-Wesley Longman Publishing Co., Inc.)

Alvarez, M. A., Bromm, V., & Shapiro, P. R. 2006, *ApJ*, 639, 621
 Beers, T. C., & Christlieb, N. 2005, *ARA&A*, 43, 531
 Beers, T. C., Norris, J. E., Placco, V. M., et al. 2014, *ApJ*, 794, 58
 Beers, T. C., Placco, V. M., Carollo, D., et al. 2017, *ApJ*, 835, 81
 Bessell, M. S., Collet, R., Keller, S. C., et al. 2015, *ApJL*, 806, L16
 Bonifacio, P., Caffau, E., Spite, M., et al. 2015, *A&A*, 579, A28
 Buzzoni, B., Delabre, B., Dekker, H., et al. 1984, *Msngr*, 38, 9
 Casagrande, L., Ramírez, I., Meléndez, J., Bessell, M., & Asplund, M. 2010, *A&A*, 512, A54
 Casey, A. R., & Schlafman, K. C. 2015, *ApJ*, 809, 110
 Casey, A. R., & Schlafman, K. C. 2017, *ApJ*, 850, 179
 Chakraborty, A., Feigelson, E. D., & Babu, G. J. 2014, *Astrolabe: Astronomy Users Library for R, r Package Version 0.1*
 Chiaki, G., Susa, H., & Hirano, S. 2018, *MNRAS*, 475, 4378
 Chiaki, G., Tominaga, N., & Nozawa, T. 2017, *MNRAS*, 472, L115
 Clemens, J. C., Crain, J. A., & Anderson, R. 2004, *Proc. SPIE*, 5492, 331
 Cooke, R., Pettini, M., & Murphy, M. T. 2012, *MNRAS*, 425, 347
 Davies, R. L., Allington-Smith, J. R., Bettess, P., et al. 1997, *Proc. SPIE*, 2871, 1099
 Demarque, P., Woo, J.-H., Kim, Y.-C., & Yi, S. K. 2004, *ApJS*, 155, 667
 Dotter, A., Chaboyer, B., Jevremović, D., et al. 2008, *ApJS*, 178, 89
 Drout, M. R., Piro, A. L., Shappee, B. J., et al. 2017, *Sci*, 358, 1570
 Frebel, A. 2018, *ARNPS*, 68, 237
 Frebel, A., Simon, J. D., & Kirby, E. N. 2014, *ApJ*, 786, 74
 Gimeno, G., Roth, K., Chiboucas, K., et al. 2016, *Proc. SPIE*, 9908, 99082S
 Gull, M., Frebel, A., Cain, M. G., et al. 2018, *ApJ*, 862, 174
 Hansen, T., Hansen, C. J., Christlieb, N., et al. 2015, *ApJ*, 807, 173
 Hansen, T. T., Andersen, J., Nordström, B., et al. 2016, *A&A*, 586, A160
 Hansen, T. T., Holmbeck, E. M., Beers, T. C., et al. 2018, *ApJ*, 858, 92
 Hartwig, T., Yoshida, N., Magg, M., et al. 2018, *MNRAS*, 478, 1795
 Henden, A., & Munari, U. 2014, *CoSka*, 43, 518
 Holmbeck, E. M., Beers, T. C., Roederer, I. U., et al. 2018, *ApJL*, 859, L24
 Ito, H., Aoki, W., Beers, T. C., et al. 2013, *ApJ*, 773, 33
 Jeon, M., Besla, G., & Bromm, V. 2017, *ApJ*, 848, 85
 Keller, S. C., Bessell, M. S., Frebel, A., et al. 2014, *Natur*, 506, 463
 Kordopatis, G., Gilmore, G., Steinmetz, M., et al. 2013, *AJ*, 146, 134
 Lee, Y. S., Beers, T. C., Allende Prieto, C., et al. 2011, *AJ*, 141, 90
 Lee, Y. S., Beers, T. C., Masseron, T., et al. 2013, *AJ*, 146, 132
 Lee, Y. S., Beers, T. C., Sivarani, T., et al. 2008a, *AJ*, 136, 2022
 Lee, Y. S., Beers, T. C., Sivarani, T., et al. 2008b, *AJ*, 136, 2050
 Martini, P., Elias, J., Points, S., et al. 2014, *Proc. SPIE*, 9147, 91470Z
 McMahon, L. E. 1974, *SED: A Non-interactive Text Editor* <http://sed.sourceforge.net>
 Nordlander, T., Amarsi, A. M., Lind, K., et al. 2017, *A&A*, 597, A6
 Norris, J. E., Yong, D., Bessell, M. S., et al. 2013, *ApJ*, 762, 28
 Placco, V. M., Beers, T. C., Ivans, I. I., et al. 2015a, *ApJ*, 812, 109
 Placco, V. M., Beers, T. C., Reggiani, H., & Meléndez, J. 2016a, *ApJL*, 829, L24
 Placco, V. M., Beers, T. C., Roederer, I. U., et al. 2014a, *ApJ*, 790, 34
 Placco, V. M., Beers, T. C., Santucci, R. M., et al. 2018, *AJ*, 155, 256
 Placco, V. M., Frebel, A., Beers, T. C., et al. 2016b, *ApJ*, 833, 21
 Placco, V. M., Frebel, A., Beers, T. C., & Stancliffe, R. J. 2014b, *ApJ*, 797, 21
 Placco, V. M., Frebel, A., Lee, Y. S., et al. 2015b, *ApJ*, 809, 136
 Placco, V. M., Holmbeck, E. M., Frebel, A., et al. 2017, *ApJ*, 844, 18
 R Core Team 2015, *R: A Language and Environment for Statistical Computing*, R Foundation for Statistical Computing, Vienna, Austria
 Reggiani, H., Meléndez, J., Kobayashi, C., Karakas, A., & Placco, V. 2017, *A&A*, 608, A46
 Rocha-Pinto, H. J. 2014, *AitoffR v0.1: Aitoff Projections in R*
 Roederer, I. U., Lawler, J. E., Cowan, J. J., et al. 2012a, *ApJL*, 747, L8
 Roederer, I. U., Lawler, J. E., Sobeck, J. S., et al. 2012b, *ApJS*, 203, 27
 Roederer, I. U., Placco, V. M., & Beers, T. C. 2016, *ApJL*, 824, L19
 Roederer, I. U., Sakari, C. M., Placco, V. M., et al. 2018, *ApJ*, 865, 129
 Roederer, I. U., Schatz, H., Lawler, J. E., et al. 2014, *ApJ*, 791, 32
 Sakari, C. M., Placco, V. M., Farrell, E. M., et al. 2018a, *ApJ*, 868, 110
 Sakari, C. M., Placco, V. M., Hansen, T., et al. 2018b, *ApJL*, 854, L20
 Schlafly, E. F., & Finkbeiner, D. P. 2011, *ApJ*, 737, 103
 Schlafman, K. C., & Casey, A. R. 2014, *ApJ*, 797, 13
 Schöreck, T., Christlieb, N., Cohen, J. G., et al. 2009, *A&A*, 507, 817
 Shappee, B. J., Simon, J. D., Drout, M. R., et al. 2017, *Sci*, 358, 1574
 Skrutskie, M. F., Cutri, R. M., Stiening, R., et al. 2006, *AJ*, 131, 1163
 Snenen, C., McWilliam, A., Preston, G. W., et al. 1996, *ApJ*, 467, 819
 Snenen, C., Preston, G. W., McWilliam, A., & Searle, L. 1994, *ApJL*, 431, L27
 Spite, M., Caffau, E., Bonifacio, P., et al. 2013, *A&A*, 552, A107
 Steinmetz, M., Zwitter, T., Siebert, A., et al. 2006, *AJ*, 132, 1645
 Tody, D. 1986, *Proc. SPIE*, 627, 733

Tody, D. 1993, in ASP Conf. Ser. 52, *Astronomical Data Analysis Software and Systems II*, ed. R. J. Hanisch, R. J. V. Brissenden, & J. Barnes (San Francisco, CA: ASP), 173

Williams, T., & Kelley, C. 2015, *Gnuplot 5.0: An Interactive Plotting Program*, <http://www.gnuplot.info/>

Wilson, E. B. 1927, *J. Am. Stat. Assoc.*, 22, 209

Wright, E. L., Eisenhardt, P. R. M., Mainzer, A. K., et al. 2010, *AJ*, 140, 1868

Yong, D., Norris, J. E., Bessell, M. S., et al. 2013, *ApJ*, 762, 27

Yoon, J., Beers, T. C., Dietz, S., et al. 2018, *ApJ*, 861, 146

Yoon, J., Beers, T. C., Placco, V. M., et al. 2016, *ApJ*, 833, 20

Youakim, K., Starkenburg, E., Aguado, D. S., et al. 2017, *MNRAS*, 472, 2963

Zacharias, N., Finch, C. T., Girard, T. M., et al. 2013, *AJ*, 145, 44